Frontiers of Physics
https://doi.org/10.1007/s11467-021-1143-0
Front. Phys.
17(4), 43503 (2022)

RESEARCH ARTICLE

Theoretical study of broadband near-field optical spectrum of twisted bilayer graphene

Lu Wen[1], Yijun Liu[2], Guoyu Luo[1], Xinyu Lv[1], Kaiyuan Wang[2], Wang Zhu[2], Lei Wang[2], Zhiqiang Li[1,†]

[1] *College of Physics, Sichuan University, Chengdu 610064, China*
[2] *National Laboratory of Solid-State Microstructures, School of Physics, Nanjing University, Nanjing 210093, China*
Corresponding author. E-mail: [†] *zhiqiangli@scu.edu.cn*
Received November 4, 2021; accepted January 6, 2022

We theoretically study the broadband near-field optical spectrum of twisted bilayer graphene (TBG) at various twist angles near the magic angle using two different models. The spectrum at low Fermi energy is characterized by a series of peaks that are almost at the same energies as the peaks in the far-field optical conductivity of TBG. When the Fermi energy is near a van Hove singularity, an additional strong peak appears at finite energy in the near-field spectrum, which has no counterpart in the optical conductivity. Based on a detailed calculation of the plasmon dispersion, we show that these spectroscopic features are associated with interband and intraband plasmons, which can provide critical information about the local band structure and plasmonic excitations in TBG. The near-field peaks evolve systematically with the twist angle, so they can serve as fingerprints for identifying the spatial dependent twist angle in TBG samples. Our findings pave the way for future experimental studies of the novel optical properties of TBG in the nanoscale.

Keywords twisted bilayer graphene, SNOM, broadband near-field optical spectrum, optical conductivity, magic angle

1 Introduction

The recent discoveries of Mott insulator phase [1–3], superconductivity [4–7] and many topological phenomena [8, 9] in twisted bilayer graphene (TBG) have generated great interest in this system. These new findings are associated with the formation of flat bands near the so-called magic twist angle near 1.05° [10, 11]. The band structure of TBG and the observed new electronic phases show critical dependence on the twist angle, which generally changes spatially in realistic samples due to strain and wrinkles induced during the fabrication process and by the substrate. Moreover, significant atomic scale lattice relaxations are observed in TBG due to the competition between interlayer van der Waals interaction and intralayer lattice distortion [12–17], which is also spatially dependent and significantly changes the local band structure and properties. Therefore, it is of great importance to explore the physics of TBG using imaging techniques with high spatial resolution.

Over the past decade, broadband near-field infrared (IR) spectroscopy based on scattering type scanning near-field optical microscopy (s-SNOM) has emerged as a powerful technique to study a wide variety of new physical phenomena in the nanometer scale [18–29]. The IR regime is of great interest for exploring TBG, because the energy scales of many physical phenomena and electronic excitations in graphene systems lie in this energy range, including interband transitions, band gap, many body interactions and collective modes [30]. Broadband SNOM can provide point-by-point near-field spectral information with spatial resolution of about 20 nm. Optical measurements with such high resolution are particularly important for probing the local band structure and electronic properties of TBG because the twist angle and atomic lattice reconstruction show large spatial dependence in realistic samples [31, 32]. While the far-field optical conductivity of TBG has been studied theoretically and experimentally in several previous works [33–35], the broadband near-field optical spectrum of TBG is yet to be explored so far.

In this work, we present a theoretical study of the broadband near-field optical spectra of TBG on top of SiO_2 substrate with different Fermi energies (E_F) and twist angles in comparison with the optical conductivity spectra. Interestingly, we find that the features in the near-field spectrum at $E_F = 0$ closely resemble the peaks in the optical conductivity of TBG. When Fermi level is near the van Hove singularity, a strong resonance peak appears at

* Special Topic: Two-dimensional Layered Materials and Device Physics (Ed. Lei Wang). This article can also be found at http://journal.hep.com.cn/fop/EN/10.1007/s11467-021-1143-0.

finite energy in the near-field spectrum, which is absent in the optical conductivity. Based on a detailed calculation of the dispersion of TBG plasmons, our analysis shows that these near-field spectroscopic features arise from intraband and interband plasmons in TBG, all of which evolve systematically with the twist angle. We show that calculations employing two different models produce similar near-field spectra.

2 Theoretical model

Figure 1(a) displays a schematic of the near-field analysis used to study the TBG on top of SiO_2 substrate. The Brillouin zone of TBG with a small rotation angle θ is shown in Fig. 1(b). The large hexagons in red and blue represent the first Brillouin zone of the upper and lower monolayer, respectively. K_l and K_l' denote the two inequivalent valleys of layer l ($l = 1, 2$ corresponds to the upper and lower layer, respectively). The small black hexagon represents the mini-Brillouin zone resulting from the difference between the two K (K') wavevectors. K_s, K_s', M_s, Γ_s correspond to points in the mini-Brillouin zone.

In our theoretical model, the TBG/SiO_2 structure in Fig. 1(a) is treated as a layered medium consisting of two regions: vacuum and SiO_2. The TBG layer at the twisted angle $\theta = 1.05°$ is considered a two-dimensional (2D) layer regardless of thickness, which has the sheet conductivity $\sigma(\omega)$ given by the Kubo formula:

$$\sigma(\omega) = \frac{e^2\hbar}{\mathrm{i}S}\sum_{m,n}\frac{f(E_m) - f(E_n)}{E_m - E_n}\frac{|\langle a_m|v_x|a_n\rangle|^2}{\hbar\omega + \mathrm{i}\eta - E_n + E_m}, \tag{1}$$

where S is the area of the TBG system in real space, $f(E)$ is the Fermi distribution function, v_x represents the velocity operator, η is the phenomenological broadening, which is 0.003 eV [35], and $\hbar\omega$ is the incident photon energy. The eigenenergy $E_m(E_n)$ and eigenstate $|a_m\rangle$ ($|a_n\rangle$) are obtained by solving the Hamiltonian of TBG based on the effective continuum model [35–38], which also takes into account the effects of lattice relaxation in TBG system. More rigorous mathematical details can be found in Refs. [35–38]. Furthermore, to calculate the imaginary part of the conductivity in TBG, because it involves summation over the entire energy band, we make use of the Kramers–Kronig (KK) relation [39]. Thus, the imaginary part can be written as

$$\mathrm{Im}\,\sigma(\omega) = \frac{2}{\pi\omega}\left(P\int_0^{\Lambda}\mathrm{d}v\frac{v^2\,\mathrm{Re}\,\sigma(v)}{\omega^2 - v^2} + 2\Lambda\right) + \frac{2}{\pi}\log\left(\frac{\Lambda - \omega}{\Lambda + \omega}\right). \tag{2}$$

In Eq. (2), P denotes the Cauchy principal value, and Λ is a finite cut-off frequency due to the fact that the Re $\sigma(\omega)$ tends to a relatively constant at high frequencies.

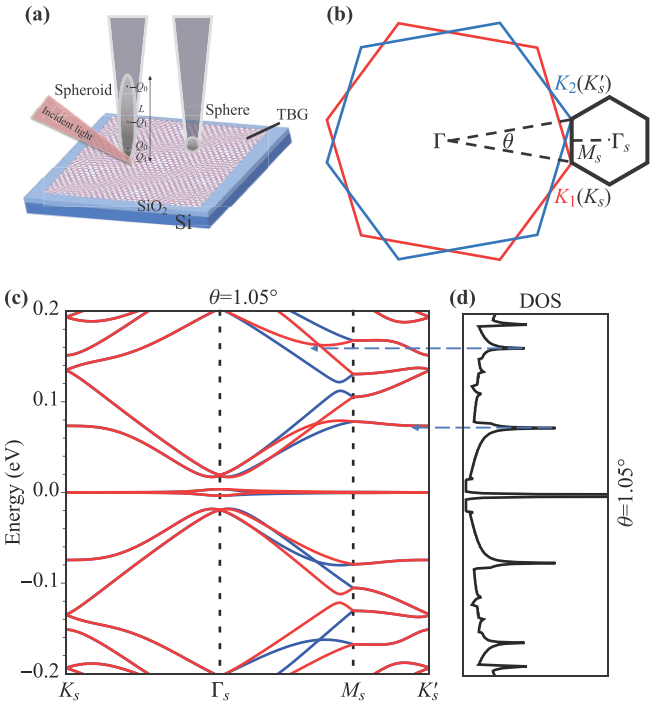

Fig. 1 **(a)** Illustration of the FDM and PDM. A spheroid (or sphere) represents the tip with the length L. In FDM, its polarization in the incident P polarized light is approximated by the monopoles Q_0 and $-Q_0$ forming the dipole p_0, and the near-field induced charges Q_1 and $-Q_1$ form the dipole p_1. **(b)** The moiré Brillouin zone (small black hexagon) is constructed from the difference between the two K (K') wavevectors for the two layers (red hexagon: layer 1, blue hexagon: layer 2). K_s, K_s', M_s, Γ_s correspond to points in the moiré Brillouin zone. **(c)** Band structure and **(d)** density of states (DOS) of relaxed TBG with $\theta = 1.05°$. The red line (blue line) represents the energy bands of K (K') valleys. The blue dashed arrow indicates the saddle point in the band structure corresponding to the van Hove singularity in DOS.

With decades of development, many theoretical and simulation methods have been developed for s-SNOM data analysis, including the point-dipole model (PDM) [40, 41], finite-dipole model (FDM) [42, 43], generalized spectral method (GSM) [44], and conformal mapping method (CMM) [45]. In this article, our near-field spectra calculation method follows the FDM developed previously for multilayer systems with some modifications needed to account for the 2D nature of TBG [43]. The AFM tip is approximated by a conducting metallic spheroid with the length L (about 600 nm) and the radius $\rho \approx 30$ nm, which is polarized by a homogenous external field forming the dipole p_0, as shown on the left of Fig. 1(a). The polarized apex generates evanescent fields with a large in-plane wavevector component q coupled with the sample. Based on a previous study [46], it is known that only the localized charges Q_0 near the end of the spheroid are relevant to the near-field interaction with the sample, where a charge distribution is induced in the vicinity of the sam-

ple surface. Then, the near-field is altered, which in turn has an effect on the tip polarization, inducing charges to form the dipole p_1 in the tip. Moreover, the near-filed interaction of the tip and the sample is usually treated electrostatically by introducing virtual image charges in the sample. Under this assumption, the actual geometric properties of the system are taken into account [47].

To accurately quantify the near-field interaction between the tip and the sample, we examine the frequency and momentum (q) dependent reflection coefficient $r_p(q, \omega)$ at the vacuum and TBG/SiO_2 interface, defined as the ratio of the amplitude of P-polarized reflected field E_r to that of the P-polarized incident field E_i. It is written as

$$r_p(q, \omega) = \frac{\varepsilon_1 k_0 - \varepsilon_0 k_1 + \frac{4\pi k_0 k_1 \sigma}{\omega}}{\varepsilon_1 k_0 + \varepsilon_0 k_1 + \frac{4\pi k_0 k_1 \sigma}{\omega}}, \tag{3}$$

where ε_0 is the dielectric constant of vacuum, ε_1 represents the complex dielectric function of SiO_2, and $k_j = \sqrt{\varepsilon_j(\frac{\omega}{c})^2 - q^2}$ are the out-of-plane components of momenta ($j = 0, 1$ label the vacuum and SiO_2, respectively). However, in actual experiments, the s-SNOM can probe the surface excitation of the sample most effectively when the range of in-plane momenta q is around the peak $q \approx \frac{1}{\rho} \gg \sqrt{\varepsilon_j}(\frac{\omega}{c})$. Therefore, k_j is approximated to $k_j = \sqrt{-q^2}$ in our calculation. From Eq. (3), one can see that the in-plane properties of TBG are responsible for its near-field response. When $q > 0$, $r_p\,(q,\ \omega)$ describes electrodynamics of the TBG/SiO_2 structure in the near field, namely, evanescent fields with a wide range of in-plane momenta q.

Based on the above, the propagation field containing the near-filed information back-scattered from the system is proportional to the effective polarizability α_{eff} of the spheroid-shaped tip, which is given by

$$\alpha_{eff} \propto \frac{p_1}{p_0} + 1 = \frac{1}{2}\frac{r_p(q, \omega) f_0}{1 - \beta f_1} + 1, \tag{4}$$

with

$$f_{0,1} = \left(g - \frac{\rho + 2H + W_{0,1}}{L}\right) \frac{\ln \frac{2L}{\rho + 4H + 2W_{0,1}}}{\ln \frac{2L}{\rho}}. \tag{5}$$

Here g is an empirical geometry factor, which is $0.7e^{0.06i}$ [42] in the following calculations, and $W_{0,1}$ denotes the position of point monopole in the dipole $p_{0,1}$, where $W_0 \approx 1.31\rho$ and $W_0 \approx \rho/2$ [42]. In addition, the tapping mode of the AFM probe with a mechanical resonance frequency (Ω) in s-SMON is considered in the FDM. The distance between the tip and the sample interface H is $H(t) = H_0 + A(1 + \cos\Omega t)$, where $H_0 = 0.7\rho$ is the minimum tip–sample separation, and $A = 40$ nm represents a typical tapping amplitude of tip. Finally, by calculating the Fourier component $\alpha_{eff,\,n}$ of α_{eff}, the final result for the demodulated signal is obtained, with amplitude $S_n \propto |\alpha_{eff,\,n}|$ and phase $\varphi_n \propto \arg(\alpha_{eff,\,n})$ corresponding to the respective measured signals in experiments.

3 Results and discussion

As shown in Fig. 1(c), we calculated the electronic band structure of TBG at rotation angle $\theta = 1.05°$ based on the effective continuum model. The path of band struc-

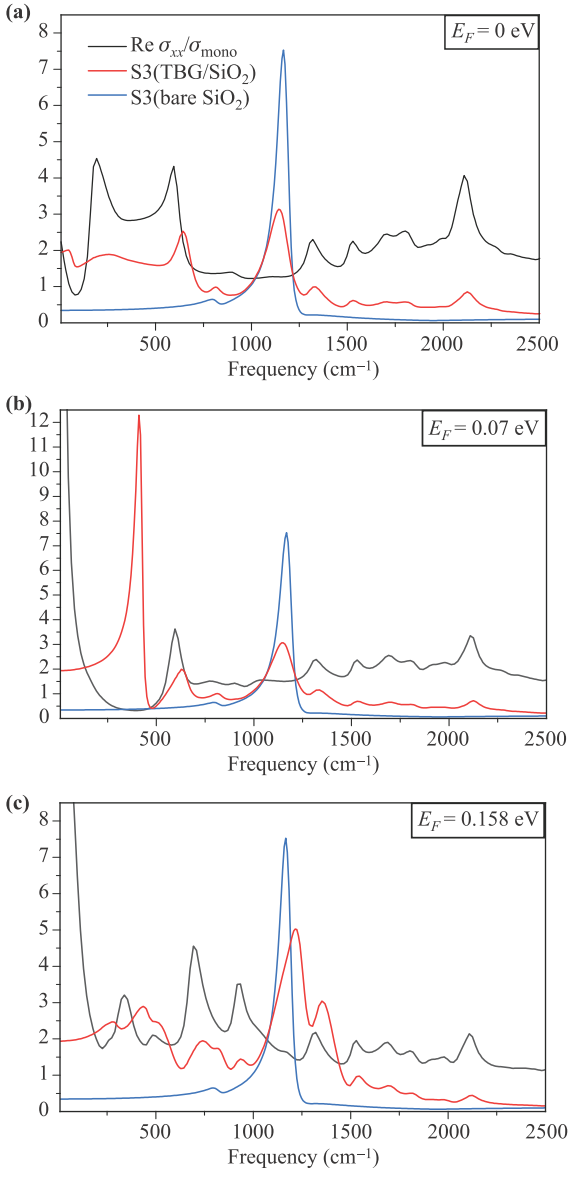

Fig. 2 The third harmonic near-field amplitude spectra $S_3(\omega)$ (red line) of TBG/SiO_2 structure together with the optical conductivity spectra $\sigma(\omega)$ (black line) of TBG at $\theta = 1.05°$ with various Fermi level **(a)** E_F= 0 eV, **(b)** E_F= 0.07 eV and **(c)** E_F= 0.158 eV, respectively. The blue line represents the near-field $S_3(\omega)$ spectra of bare SiO_2 substrate. These results are calculated at a temperature close to 4 K.

ture is along the line K_s–Γ_s–M_s–K'_s in the moiré Brillouin zone. The energy of the charge neutral point (CNP) is set to $E = 0$ eV. The red (blue) line represents the energy bands of K (K') valley. At the low energy region, the bands are very flat and the band velocity vanishes. Because of the influence of lattice relaxation, the flat bands near the Dirac point are obviously gapped from the high energy bands in both the electron side and the hole side. Additionally, each characteristic saddle point of the band structure is corresponding to a van Hove singularity in the density of states (DOS) in Fig. 1(d). As indicated by the blue dashed arrows, the large density of electron states mainly occurs in the energy range around $E = 0.075$ eV and $E = 0.163$ eV.

In Fig. 2, we show the representative near-field spectra $S_3(\omega)$ of TBG on top of SiO_2 substrate together with the optical conductivity spectra $\sigma(\omega)$ of TBG at various E_F. Here, $S_3(\omega)$ is near-field amplitude spectrum demodulated at the third harmonic of the tip tapping frequency, which are obtained by the FDM described above. In each case, the black line represents the optical conductivity spectrum of TBG in units of the dynamical conductivity of monolayer graphene $\sigma_{mono} = \frac{g_v g_s}{16}\frac{e^2}{\hbar}$, and the spin and valley degeneracy are $g_v = g_s = 2$ [48]. The blue line and red line represent the near-field spectra of bare SiO_2 substrate and TBG/SiO_2 system, respectively. As shown in Fig. 2, the conductivity spectra $\sigma(\omega)$ display numerous characteristic peaks associated with electronic interband transitions. All $S_3(\omega)$ spectra of TBG/SiO_2 structure have a strong peak around $\omega = 1064$ cm^{-1} due to the surface phonon of SiO_2. In Figs. 2(a)–(c), the $S_3(\omega)$ spectra at various Fermi levels exhibit a series of sharp peaks above 400 cm^{-1}, which are almost at the same energies as the interband transition peaks in the $\sigma(\omega)$ spectrum. When the Fermi level $E_F = 0.07$ eV approaches the first van Hove singularity $E = 0.075$ eV, the $S_3(\omega)$ spectrum in Fig. 2(b) shows a strong near-field resonance peak near $\omega \sim 400$ cm^{-1}, which is absent in $\sigma(\omega)$. For $E_F = 0.158$ eV in Fig. 2(c), the feature near $\omega \sim 400$ cm^{-1} in $S_3(\omega)$ disappears, while the other features systematically shift to higher frequencies compared to those at $E_F = 0$ eV [Fig. 2(a)] and $E_F = 0.07$ eV [Fig. 2(b)]. We will show below that the peaks in $S_3(\omega)$ arise from interband and intraband plasmons in TBG.

In order to further study the near-field electrodynamics of the TBG/SiO_2 structure, we display the imaginary part of the reflection coefficient $r_p(q, \omega)$ calculated by Eq. (3) at different E_F in Fig. 3. Such a plot is an instructive way to visualize the dispersion of graphene plasmons, which correspond to the divergences of $r_p(q, \omega)$ of the system at complex momenta [21]. As shown in Figs. 3(a)–(c), we observe several plasmon branches extending to large q-values, which display an almost constant energy–momentum dispersion in the energy range of $\omega \sim 400$–2000 cm^{-1}. It has been shown that such modes with almost constant dispersion are interband plasmons or collective excitonic oscillations in TBG [49]. The dominant in-plane momenta contributing to near-field coupling in SNOM experiments are marked by vertical black dashed lines in Fig. 3 [21]. An examination of Fig. 2 and Fig. 3 shows that the spectroscopic features above 400 cm^{-1} in the $S_3(\omega)$ spectra are at similar energies compared to the interband plasmons in the dispersion plot. Moreover, because the features in $\sigma(\omega)$ are associated with zero momentum, the qualitatively similar energies of the peaks in $\sigma(\omega)$ and $S_3(\omega)$ are consistent with the constant dispersion of the interband plasmons. Therefore, the features above 400 cm^{-1} in $S_3(\omega)$ can be attributed to interband plasmons. When E_F is close to van Hove singularities, the high free carrier density leads to strong in-

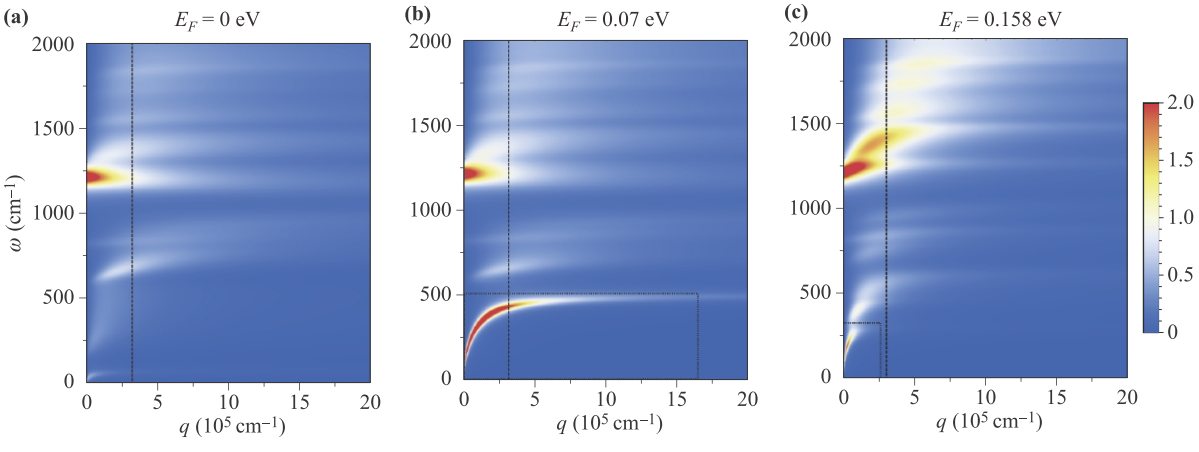

Fig. 3 Imaginary part of the reflection coefficient $r_p(q, \omega)$ with different Fermi level **(a)** $E_F = 0$ eV, **(b)** $E_F = 0.07$ eV and **(c)** $E_F = 0.158$ eV, respectively and displayed in false color scale. The temperature is close to 4 K. Vertical black dashed lines in (a–c) mark the dominant q ($\sim 3.3 \times 10^5$ cm^{-1}) for maximum near-field coupling. The black dotted boxes in (b and c) mark the intraband plasmon branches in dispersion plot.

traband plasmons [Fig. 3(b)], which are observed in the low frequency region ($\omega < 400$ cm^{-1}) where the plasmon mode has a $\omega \propto \sqrt{q}$ dispersion at low energy as expected for 2D electronic systems, as shown in the black dotted box. Based on the energy of the intraband plasmons at the dominant in-plane momenta contributing to near-field coupling, the peak near $\omega \sim 400$ cm^{-1} in the $S_3(\omega)$ spectrum in Fig. 2(b) can be assigned to intraband plasmons. For $E_F = 0.158$ eV, the resonance amplitude of intraband plasmons in the dispersion plot [Fig. 3(c)] is very small because of the lower free carrier density, thus it is not visible in the $S_3(\omega)$ spectrum in Fig. 2(c). Therefore, combining Fig. 2 and Fig. 3, we have shown that the features in the near-field spectra of TBG arise from intraband and interband plasmons. Because the interband plasmon features in $S_3(\omega)$ are intimately related to interband transitions, the $S_3(\omega)$ spectrum can provide critical information about the local band structure and collective excitations in TBG.

Next, in Fig. 4, we compare the near-field spectra $S_3(\omega)$ of TBG/SiO_2 structure calculated by the finite dipole model (FDM) and the point dipole model (PDM) by modelling the apex of the tip as a point dipole [21, 40, 41], as shown in right side of Fig. 1(a). After the vertical lines cut along the dominant in-plane momenta (black dashed lines) in Fig. 3, we find that the energy of each peak in the $S_3(\omega)$ spectra obtained by FDM [Fig. 4(a)] has better agreement with the plasmon energy in the dispersion plot comparing these two models. In addition, the peak energies in $S_3(\omega)$ spectra evolve systematically with the Fermi level. The characteristic peaks from interband plasmons are similar at moderate levels of carrier density ($E_F = 0$ eV and $E_F = 0.07$ eV), whereas increasing the carrier density ($E_F = 0.158$ eV) leads to drastic changes in the SiO_2

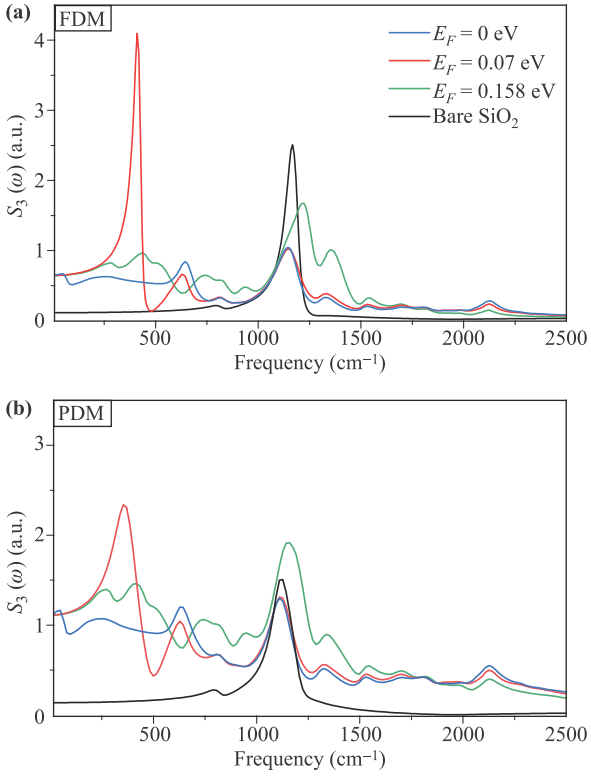

Fig. 4 The broadband near-field optical spectra $S_3\omega$) of TBG/SiO_2 structure at $\theta = 1.05°$ with various Fermi levels ($E_F = 0$ eV, 0.07 eV and 0.158 eV) using two different models, namely **(a)** FDM and **(b)** PDM, respectively. These results are obtained at a temperature close to 4 K. The black line in (a) and (b) represents the near-field spectra $S_3(\omega)$ of bare SiO_2 substrate.

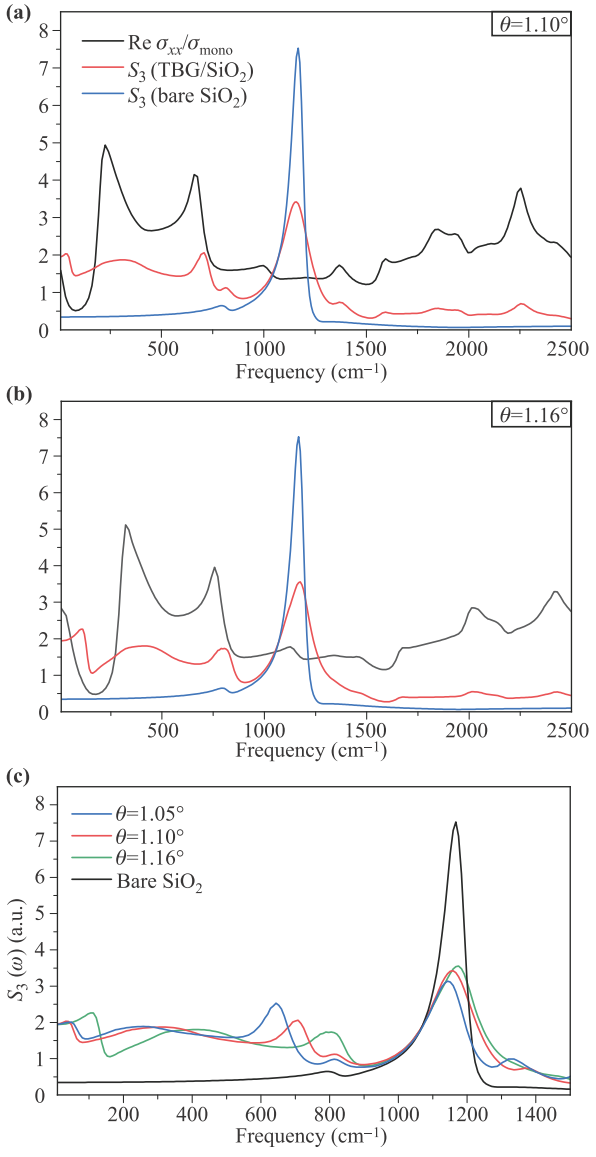

Fig. 5 The third harmonic near-field amplitude spectra $S_3(\omega)$ (red line) of TBG/SiO_2 substrate together with the optical conductivity spectra $\sigma(\omega)$ (black line) of TBG at $E_F = 0$ eV with various angle **(a)** $\theta = 1.10°$ and **(b)** $\theta = 1.16°$. The blue line in (a) and (b) represents the near-field spectra $S_3(\omega)$ of bare SiO_2 substrate. **(c)** The dependence of the near-field response of TBG/SiO_2 structure on various twist angles θ.

resonance peak around $\omega = 1064$ cm^{-1}, which originates from plasmon–phonon coupling at the graphene and SiO_2 interface. Importantly, the $S_3(\omega)$ spectra obtained from FDM and PDM models are in good agreement, including the features due to intraband and interband plasmons.

To explore the dependence of the near-field response of TBG/SiO_2 structure on twisted angle θ, in Fig. 5, we plot the $S_3(\omega)$ spectra and the far-field optical conductivity with two other rotation angles (θ =1.10° and 1.16°) at $E_F = 0$ eV. As shown in Fig. 2(a) and Figs. 5(a) and (b), the peaks due to interband transitions in $\sigma(\omega)$ spectra (black lines) almost systematically evolve with the rotation angle θ. Remarkably, in Fig. 5(c), the peaks associated with the interband plasmons in the $S_3(\omega)$ spectra (red lines) also systematically shift to higher energies with increasing rotation angle, while the intensity of the peak around $\omega \sim 650$ cm^{-1} decreases. The interband plasmon features in $S_3(\omega)$ are intimately related to interband transitions that are strongly dependent on the twist angle [33–35], therefore, these near-field features can serve as fingerprints for identifying the spatial dependent twist angle in TBG samples.

4 Conclusion

We have demonstrated that the broadband near-field optical spectrum of TBG exhibits a series of peaks originated from interband and intraband plasmons. The near-field peaks due to interband plasmons are closely related to the interband transition peaks in the optical conductivity spectrum, which is consistent with the constant dispersion of the interband plasmons. A strong peak due to intraband plasmons appears in the near-field spectrum when the Fermi level is near a van Hove singularity. The plasmons in TBG have many novel quantum properties that may lead to possible applications such as a "perfect" lens without the need of lefthanded materials. Our findings suggest that the broadband near-field optical measurements can provide critical information about TBG plasmons, including their dispersion, spectral properties as well as their twist-angle dependence.

The dependence of different peaks in the near-field spectrum on the rotation angle is explored in this article, which can be used as fingerprints to identify the twist angle in actual samples. Moreover, the spectroscopic information from such measurements will be an important means for studying the spatial dependent band structure and electronic phases of TBG samples because of the spatial variation of the twist angle. In particular, the broadband spectrum can possibly provide information on the band gap, many body interaction and collective modes of the novel electronic phases in TBG, which will be a subject of future studies. Our work has shown that broadband SNOM experiment is a very valuable approach for exploring the novel physics of TBG at the nanoscale. Besides, the model (including FDM and PDM) presented in this paper can also be used to handle other 2D layered samples, such as tri-layer graphene or other hetero-thin materials.

Acknowledgements We acknowledge the financial support from the National Natural Science Foundation of China (Grant No. 11874271).

References

1. Y. Cao, V. Fatemi, A. Demir, S. Fang, S. L. Tomarken, J. Y. Luo, J. D. Sanchez-Yamagishi, K. Watanabe, T. Taniguchi, E. Kaxiras, R. C. Ashoori, and P. Jarillo-Herrero, Correlated insulator behaviour at half-filling in magic-angle graphene superlattices, *Nature* 556(7699), 80 (2018)
2. Y. Jiang, X. Lai, K. Watanabe, T. Taniguchi, K. Haule, J. Mao, and E. Y. Andrei, Charge order and broken rotational symmetry in magic-angle twisted bilayer graphene, *Nature* 573(7772), 91 (2019)
3. A. Kerelsky, L. J. Mc Gilly, D. M. Kennes, L. Xian, M. Yankowitz, S. Chen, K. Watanabe, T. Taniguchi, J. Hone, C. Dean, A. Rubio, and A. N. Pasupathy, Maximized electron interactions at the magic angle in twisted bilayer graphene, *Nature* 572(7767), 95 (2019)
4. Y. Cao, V. Fatemi, S. Fang, K. Watanabe, T. Taniguchi, E. Kaxiras, and P. Jarillo-Herrero, Unconventional superconductivity in magic-angle graphene superlattices, *Nature* 556(7699), 43 (2018)
5. M. Yankowitz, S. Chen, H. Polshyn, Y. Zhang, K. Watanabe, T. Taniguchi, D. Graf, A. F. Young, and C. R. Dean, Tuning superconductivity in twisted bilayer graphene, *Science* 363(6431), 1059 (2019)
6. X. Lu, P. Stepanov, W. Yang, M. Xie, M. A. Aamir, I. Das, C. Urgell, K. Watanabe, T. Taniguchi, G. Zhang, A. Bachtold, A. H. MacDonald, and D. K. Efetov, Superconductors, orbital magnets and correlated states in magic-angle bilayer graphene, *Nature* 574(7780), 653 (2019)
7. Y. Xie, B. Lian, B. Jäck, X. Liu, C. L. Chiu, K. Watanabe, T. Taniguchi, B. A. Bernevig, and A. Yazdani, Spectroscopic signatures of many-body correlations in magic-angle twisted bilayer graphene, *Nature* 572(7767), 101 (2019)
8. M. Serlin, C. L. Tschirhart, H. Polshyn, Y. Zhang, J. Zhu, K. Watanabe, T. Taniguchi, L. Balents, and A. F. Young, Intrinsic quantized anomalous Hall effect in a moire heterostructure, *Science* 367(6480), 900 (2020)
9. A. L. Sharpe, E. J. Fox, A. W. Barnard, J. Finney, K. Watanabe, T. Taniguchi, M. A. Kastner, and D. Goldhaber-Gordon, Emergent ferromagnetism near three-quarters filling in twisted bilayer graphene, *Science* 365(6453), 605 (2019)
10. R. Bistritzer and A. H. MacDonald, Moire bands in twisted double-layer graphene, *Proc. Natl. Acad. Sci. USA* 108(30), 12233 (2011)

11. E. Suárez Morell, J. D. Correa, P. Vargas, M. Pacheco, and Z. Barticevic, Flat bands in slightly twisted bilayer graphene: Tight-binding calculations, *Phys. Rev. B* 82(12), 121407 (2010)
12. H. Yoo, R. Engelke, S. Carr, S. Fang, K. Zhang, P. Cazeaux, S. H. Sung, R. Hovden, A. W. Tsen, T. Taniguchi, K. Watanabe, G. C. Yi, M. Kim, M. Luskin, E. B. Tadmor, E. Kaxiras, and P. Kim, Atomic and electronic reconstruction at the van der Waals interface in twisted bilayer graphene, *Nat. Mater.* 18(5), 448 (2019)
13. S. Y. Dai, Y. Xiang, and D. J. Srolovitz, Twisted bilayer graphene: Moire with a twist, *Nano Lett.* 16(9), 5923 (2016)
14. N. N. T. Nam and M. Koshino, Lattice relaxation and energy band modulation in twisted bilayer graphene, *Phys. Rev. B* 96(7), 075311 (2017)
15. N. Y. Kim, H. Y. Jeong, J. H. Kim, G. Kim, H. S. Shin, and Z. Lee, Evidence of local commensurate state with lattice match of graphene on hexagonal boron nitride, *ACS Nano* 11(7), 7084 (2017)
16. M. M. van Wijk, A. Schuring, M. I. Katsnelson, and A. Fasolino, Relaxation of moiré patterns for slightly misaligned identical lattices: Graphene on graphite, *2D Mater.* 2, 034010 (2015)
17. F. Gargiulo and O. V. Yazyev, Structural and electronic transformation in low-angle twisted bilayer graphene, *2D Mater.* 5, 015019 (2017)
18. X. Chen, D. Hu, R. Mescall, G. You, D. N. Basov, Q. Dai, and M. Liu, Modern scattering-type scanning near-field optical microscopy for advanced material research, *Adv. Mater.* 31(24), 1804774 (2019)
19. A. J. Huber, J. Wittborn, and R. Hillenbrand, Infrared spectroscopic near-field mapping of single nanotransistors, *Nanotechnology* 21(23), 235702 (2010)
20. G. Dominguez, A. S. Mcleod, Z. Gainsforth, P. Kelly, H. A. Bechtel, F. Keilmann, A. Westphal, M. Thiemens, and D. N. Basov, Nanoscale infrared spectroscopy as a non-destructive probe of extraterrestrial samples, *Nat. Commun.* 5(1), 5445 (2014)
21. Z. Fei, G. O. Andreev, W. Bao, L. M. Zhang, A. S. Mc Leod, C. Wang, M. K. Stewart, Z. Zhao, G. Dominguez, M. Thiemens, M. M. Fogler, M. J. Tauber, A. H. Castro-Neto, C. N. Lau, F. Keilmann, and D. N. Basov, Infrared nanoscopy of Dirac plasmons at the graphene–SiO_2 interface, *Nano Lett.* 11(11), 4701 (2011)
22. S. Dai, Q. Ma, M. K. Liu, T. Andersen, Z. Fei, M. D. Goldflam, M. Wagner, K. Watanabe, T. Taniguchi, M. Thiemens, F. Keilmann, G. C. A. M. Janssen, S. E. Zhu, P. Jarillo-Herrero, M. M. Fogler, and D. N. Basov, Graphene on hexagonal boron nitride as a tunable hyperbolic metamaterial, *Nat. Nanotechnol.* 10(8), 682 (2015)
23. J. M. Stiegler, Y. Abate, A. Cvitkovic, Y. E. Romanyuk, A. J. Huber, S. R. Leone, and R. Hillenbrand, Nanoscale infrared absorption spectroscopy of individual nanoparticles enabled by scattering-type near-field microscopy, *ACS Nano* 5(8), 6494 (2011)
24. Z. Nuño, B. Hessler, B. Heiberg, R. Damato, T. Dunlap, Y. S. Shon, and Y. Abate, Nanoscale near-field infrared spectroscopic imaging of silica-shell/gold-core and pure silica nanoparticles, *J. Nanopart. Res.* 14(3), 766 (2012)
25. I. Amenabar, S. Poly, M. Goikoetxea, W. Nuansing, P. Lasch, and R. Hillenbrand, Hyperspectral infrared nanoimaging of organic samples based on Fourier transform infrared nanospectroscopy, *Nat. Commun.* 8(1), 14402 (2017)
26. M. Liu, A. J. Sternbach, M. Wagner, T. V. Slusar, T. Kong, S. L. Bud'ko, S. Kittiwatanakul, M. M. Qazilbash, A. Mc Leod, Z. Fei, E. Abreu, J. Zhang, M. Goldflam, S. Dai, G. X. Ni, J. Lu, H. A. Bechtel, M. C. Martin, M. B. Raschke, R. D. Averitt, S. A. Wolf, H. T. Kim, P. C. Canfield, and D. N. Basov, Phase transition in bulk single crystals and thin films of VO_2 by nanoscale infrared spectroscopy and imaging, *Phys. Rev. B* 91(24), 245155 (2015)
27. Z. Shi, X. Hong, H. A. Bechtel, B. Zeng, M. C. Martin, K. Watanabe, T. Taniguchi, Y. R. Shen, and F. Wang, Observation of a Luttinger-liquid plasmon in metallic single-walled carbon nanotubes, *Nat. Photon.* 9(8), 515 (2015)
28. Z. Shi, H. A. Bechtel, S. Berweger, Y. Sun, B. Zeng, C. Jin, H. Chang, M. C. Martin, M. B. Raschke, and F. Wang, Amplitude- and phase-resolved nanospectral imaging of phonon polaritons in hexagonal boron nitride, *ACS Photon.* 2(7), 790 (2015)
29. H. A. Bechtel, E. A. Muller, R. L. Olmon, M. C. Martin, and M. B. Raschke, Ultrabroadband infrared nanospectroscopic imaging, *Proc. Natl. Acad. Sci. USA* 111(20), 7191 (2014)
30. D. N. Basov, M. M. Fogler, A. Lanzara, F. Wang, and Y. Zhang, Colloquium: Graphene spectroscopy, *Rev. Mod. Phys.* 86(3), 959 (2014)
31. A. Uri, S. Grover, Y. Cao, J. A. Crosse, K. Bagani, D. Rodan-Legrain, Y. Myasoedov, K. Watanabe, T. Taniguchi, P. Moon, M. Koshino, P. Jarillo-Herrero, and E. Zeldov, Mapping the twist-angle disorder and Landau levels in magic-angle graphene, *Nature* 581(7806), 47 (2020)
32. N. P. Kazmierczak, M. Van Winkle, C. Ophus, K. C. Bustillo, S. Carr, H. G. Brown, J. Ciston, T. Taniguchi, K. Watanabe, and D. K. Bediako, Strain fields in twisted bilayer graphene, *Nat. Mater.* 20(7), 956 (2021)
33. L. Wen, Z. Li, and Y. He, Optical conductivity of twisted bilayer graphene near the magic angle, *Chin. Phys. B* 30(1), 017303 (2021)
34. Z. B. Dai, Y. He, and Z. Li, Effects of heterostrain and lattice relaxation on the optical conductivity of twisted bilayer graphene, *Phys. Rev. B* 104(4), 045403 (2021)
35. P. Moon and M. Koshino, Optical absorption in twisted bilayer graphene, *Phys. Rev. B* 87(20), 205404 (2013)
36. J. M. B. Lopes dos Santos, N. M. R. Peres, and A. H. Castro Neto, Continuum model of the twisted graphene bilayer, *Phys. Rev. B* 86(15), 155449 (2012)
37. M. Koshino, N. F. Q. Yuan, T. Koretsune, M. Ochi, K. Kuroki, and L. Fu, Maximally localized wannier orbitals and the extended hubbard model for twisted bilayer graphene, *Phys. Rev. X* 8(3), 031087 (2018)

38. Z. Bi, N F Q. Yuan, and L. Fu, Designing flat bands by strain, *Phys. Rev. B* 100(3), 035448 (2019)
39. T. Stauber, P. San-Jose, and L. Brey, Optical conductivity, Drude weight and plasmons in twisted graphene bilayers, *New J. Phys.* 15(11), 113050 (2013)
40. R. Hillenbrand and F. Keilmann, Complex optical constants on a subwavelength scale, *Phys. Rev. Lett.* 85(14), 3029 (2000)
41. R. Hillenbrand, B. Knoll, and F. Keilmann, Pure optical contrast in scattering-type scanning near-field microscopy, *J. Microsc.* 202, 77 (2001)
42. A. Cvitkovic, N. Ocelic, and R. Hillenbrand, Analytical model for quantitative prediction of material contrasts in scattering-type near-field optical microscopy, *Opt. Express* 15(14), 8550 (2007)
43. B. Hauer, A. Engelhardt, and T. Taubner, Quasi-analytical model for scattering infrared near-field microscopy on layered systems, *Opt. Express* 20(12), 13173 (2012)
44. B. Y. Jiang, L. M. Zhang, A. H. Castro Neto, D. N. Basov, and M. M. Fogler, Generalized spectral method for near-field optical microscopy, *J. Appl. Phys.* 119(5), 054305 (2016)
45. S. T. Chui, X. Chen, M. Liu, Z. Lin, and J. Zi, Scattering of electromagnetic waves from a cone with conformal mapping: Application to scanning near-field optical microscope, *Phys. Rev. B* 97(8), 081406 (2018)
46. I. V. Lindell and K. I. Nikoskinen, Electrostatic image theory for the dielectric prolate spheroid, *J. Electromagn. Waves Appl.* 15(8), 1075 (2001)
47. S. Amarie and F. Keilmann, Broadband-infrared assessment of phonon resonance in scattering-type near-field microscopy, *Phys. Rev. B* 83(4), 045404 (2011)
48. V. P. Gusynin and S. G. Sharapov, Transport of Dirac quasiparticles in graphene: Hall and optical conductivities, *Phys. Rev. B* 73(24), 245411 (2006)
49. T. Stauber and H. Kohler, Quasi-flat plasmonic bands in twisted bilayer graphene, *Nano Lett.* 16(11), 6844 (2016)